

Towards a robust R2D2 paradigm for radio-interferometric imaging: revisiting DNN training and architecture

AMIR AGHABIGLOU,¹ CHUNG SAN CHU,¹ CHAO TANG,^{1,2} ARWA DABBECH,¹ AND YVES WIAUX¹

¹*Institute of Sensors, Signals and Systems, Heriot-Watt University, Edinburgh EH14 4AS, United Kingdom*

²*EPCC, University of Edinburgh, Potterrow, Edinburgh EH8 9BT, United Kingdom*

ABSTRACT

The R2D2 Deep Neural Network (DNN) series was recently introduced for image formation in radio interferometry. It can be understood as a learned version of CLEAN, whose minor cycles are substituted with DNNs. We revisit R2D2 on the grounds of series convergence, training methodology, and DNN architecture, improving its robustness in terms of generalisability beyond training conditions, capability to deliver high data fidelity, and epistemic uncertainty. Firstly, while still focusing on telescope-specific training, we enhance the learning process by randomising Fourier sampling integration times, incorporating multi-scan multi-noise configurations, and varying imaging settings, including pixel resolution and visibility-weighting scheme. Secondly, we introduce a convergence criterion whereby the reconstruction process stops when the data residual is compatible with noise, rather than simply using all available DNNs. This not only increases the reconstruction efficiency by reducing its computational cost, but also refines training by pruning out the data/image pairs for which optimal data fidelity is reached before training the next DNN. Thirdly, we substitute R2D2's early U-Net DNN with a novel architecture (U-WDSR) combining U-Net and WDSR, which leverages wide activation, dense connections, weight normalisation, and low-rank convolution to improve feature reuse and reconstruction precision. As previously, R2D2 was trained for monochromatic intensity imaging with the Very Large Array (VLA) at fixed 512×512 image size. Simulations on a wide range of inverse problems and a case study on real data reveal that the new R2D2 model consistently outperforms its earlier version in image reconstruction quality, data fidelity, and epistemic uncertainty.

Keywords: Computational methods (1965) — Neural networks (1933) — Astronomy image processing (2306) — Aperture synthesis (53)

1. INTRODUCTION

Radio Interferometry (RI) is a core data acquisition modality in radio astronomy that enables the study of intricate phenomena in the universe, such as cosmic magnetic fields, galaxy formation, and the properties of black holes. The advent of advanced radio telescopes, such as MeerKAT (Jonas 2016), the Australian Square Kilometre Array Pathfinder (ASKAP; Hotan et al. 2021), the Low-Frequency Array (LOFAR; van Haarlem et al. 2013), and the upcoming Square Kilometre Array (SKA; Labate et al. 2022; Swart et al. 2022), has pushed the field forward, offering unprecedented res-

olution and sensitivity. However, these advancements pose challenges for the image formation process, now due to scale to large data volumes while delivering the target resolution and dynamic range.

RI data consists of noisy, undersampled Fourier measurements of the target radio image. The underpinning image formation problem is an ill-posed inverse problem. Thanks to its simplicity and computational efficiency, the CLEAN algorithm (Högbon 1974) has been a long-standing standard in RI imaging. However, CLEAN's limitations become apparent when addressing complex emission and high dynamic ranges. The algorithm's reliance on a simplistic prior model can lead to suboptimal results, particularly when the required angular resolution surpasses the nominal instrumental resolution.

In response to these limitations, the field has shifted toward more advanced computational imaging tech-

niques. Algorithms grounded in optimisation theory, such as the SARA family (Carrillo et al. 2012; Onose et al. 2016, 2017; Repetti & Wiaux 2020; Terris et al. 2022), have demonstrated superior image reconstruction capabilities by incorporating handcrafted sparsity-based regularisation, enabling higher resolution and more physical reconstruction of the target signal than CLEAN. Despite their high image precision, these algorithms remain highly iterative at the target high dynamic ranges, which leads to inevitable computational limitations in large-scale regimes.

More recently, the integration of deep learning into image reconstruction has opened new avenues for enhancing both speed and precision. On the one hand, end-to-end DNNs, promising ultra-fast reconstructions, have been explored, albeit with trade-offs in robustness, generalisability, and interpretability (Connor et al. 2022; Geyer et al. 2023). On the other hand, plug-and-play (PnP) algorithms, such as AIRI (Terris et al. 2022, 2025), combine the strengths of deep learning and optimisation, offering a flexible framework by replacing regularisation terms with learned denoisers. These hybrid algorithms are also highly iterative in nature, raising concerns about their computational efficiency.

Very recently, we have introduced the R2D2—short for Residual-to-Residual DNN series for high-Dynamic-range imaging—paradigm (Aghabiglou et al. 2023, 2024; Dabbech et al. 2024), aiming to improve both precision and computational efficiency over the state of the art. R2D2 forms an image as a series of residual images iteratively estimated as outputs of DNNs, taking the previous iteration and associated data residual as inputs. R2D2 can thus be understood as a learned version of CLEAN, whose minor cycles are substituted with iteration-specific DNNs. The first incarnation of the R2D2 algorithm was underpinned by the U-Net architecture. Despite its promising precision and computational efficiency in both simulation and real data, R2D2’s robustness across diverse imaging settings was unexplored, including varying visibility-weighting schemes, pixel resolution, and image sizes. Generalising the approach from the current monochromatic intensity imaging setting to address wideband polarisation imaging is yet to be investigated.

In this paper, we build on these foundations and propose several key advancements to address the limitations of R2D2 while maintaining its focus on monochromatic intensity imaging with VLA at the image size 512×512 . These include training methodology, convergence criterion, and DNN architecture. Our contributions aim to improve R2D2’s robustness, defined in terms of general-

isability beyond training conditions, capability to deliver high data fidelity, and epistemic uncertainty.

Firstly, we generalise the training setup from Aghabiglou et al. (2024), by introducing stochastic variations in key observational and imaging parameters. In our previous study, we adopted fixed imaging settings whereby (i) the imaging pixel resolution was set to enable a fixed ratio of the imaging resolution to the nominal instrumental resolution, and (ii) the Briggs weighting scheme was applied with a fixed value of the robustness parameter which controls the trade-off between uniform and natural weighting schemes. Other observation settings such as the integration time were also fixed. In this work, we randomise all the above parameters. Additionally, we extend the algorithm to support multi-noise and multi-scan configurations, enabling it to handle more complex and realistic observational scenarios.

Secondly, we enhance the R2D2 paradigm by introducing a convergence criterion whereby the reconstruction process is deemed complete and iterations stop when the data residual is compatible with noise, rather than simply using all available DNNs. This not only reduces the training computational cost but also improves reconstruction efficiency. Concurrently, a pruning process is applied during training to both the training and validation datasets. Discarding already solved inverse problems in early R2D2 iterations allows subsequent DNNs to focus on more challenging cases, enhancing overall training efficiency and model learning.

Thirdly, we revisit the R2D2 model using a novel DNN architecture, dubbed U-WDSR (Aghabiglou et al. 2023), which combines the strengths of the U-Net architecture with WDSR residual blocks (Yu et al. 2018). The advanced architecture leverages wide activation, dense connections, and weight normalisation to improve imaging precision and robustness, enabling the recovery of finer details with enhanced data fidelity.

Furthermore, we provide a comprehensive evaluation of these contributions by benchmarking R2D2 against state-of-the-art RI imaging algorithms, namely AIRI and uSARA (Terris et al. 2022). R2D2 is implemented as a fully Python GPU-enabled algorithm. For a fair comparison, we transition both AIRI and uSARA implementations from MATLAB to GPU-enabled Python, significantly improving their computational efficiency. These GPU-accelerated implementations are integrated into BASPLib¹, a publicly available code library ded-

¹ BASPLib: The Biomedical and Astronomical Signal Processing library is available at <https://basp-group.github.io/BASPLib/>.

icated to solving imaging inverse problems. R2D2 is also benchmarked against multi-scale CLEAN from the widely-used WSClean software (Offringa et al. 2014; Offringa & Smirnov 2017).

The remainder of this paper is organised as follows. Section 2 revisits the data model for RI imaging and provides an overview of the R2D2 algorithmic structure. Section 3 delves into the training methodology for robust R2D2 algorithm, detailing the construction of a generalised training set, convergence criterion, the novel UWDSR DNN architecture, epistemic uncertainty quantification, training implementation and computational cost. Section 4 examines R2D2’s robustness and generalisability under diverse experimental setups, and evaluates its performance in comparison with the earlier R2D2 model (Aghabiglou et al. 2024) and the benchmark algorithms, with a focus on imaging precision and computational efficiency. Additionally, it explores epistemic uncertainty to further validate R2D2’s robustness. Section 5 revisits real observations of the radio galaxy Cygnus A with the new R2D2 model. Finally, Section 6 summarises the key findings and provides directions for future work.

2. R2D2 PARADIGM

This section revisits the RI data model in the context of monochromatic intensity imaging and provides an overview of R2D2 algorithmic structure.

2.1. RI data model

Under the assumption of non-polarised monochromatic radio emission, spanning a narrow field of view, RI data, also called visibilities, are incomplete noisy Fourier measurements of the intensity image of interest. Let $\mathbf{x}^* \in \mathbb{R}_+^N$ represent the unknown intensity (and thus non-negative) image of the sky, with N pixels. Formally, the RI data model reads:

$$\mathbf{y} = \Phi \mathbf{x}^* + \mathbf{n}, \quad (1)$$

where $\mathbf{y} \in \mathbb{C}^M$ is the vector of observed visibilities, and $\mathbf{n} \in \mathbb{C}^M$ is the additive noise vector, typically assumed to be a complex random Gaussian noise with mean zero and variance $\tau^2 > 0$. The measurement operator $\Phi : \mathbb{R}^N \rightarrow \mathbb{C}^M$ represents the non-uniform Fourier sampling, and is modelled using the non-uniform fast Fourier transform (NUFFT, Fessler & Sutton 2003) such that $\Phi = \mathbf{G}\mathbf{F}\mathbf{Z}$, where $\mathbf{G} \in \mathbb{C}^{M \times D}$ is a sparse interpolation matrix, $\mathbf{F} \in \mathbb{C}^{D \times D}$ is the 2D discrete Fourier transform, and $\mathbf{Z} \in \mathbb{R}^{D \times N}$ is a zero-padding operator which also includes the correction for the convolution in the Fourier domain through \mathbf{G} . Often, a visibility-weighting scheme (e.g. Briggs weighting) is applied to

the RI data and injected into the measurement operator model to balance sensitivity and resolution depending on the target science.

The RI data model can be formulated in the image domain through a normalised back-projection via the adjoint of the measurement operator. More precisely, the back-projected data $\mathbf{x}_d \in \mathbb{R}^N$, also called the dirty image, is obtained as $\mathbf{x}_d = \kappa \text{Re}\{\Phi^\dagger \mathbf{y}\}$, where $(\cdot)^\dagger$ denotes the adjoint of its argument. The normalisation factor κ ensures that the peak value of the point spread function (PSF) is equal to one, a conventional normalisation in RI imaging. Specifically, $\kappa = \max(\text{Re}\{\Phi^\dagger \Phi \delta\})^{-1}$, where δ is an image with a value of 1 at its centre and 0 elsewhere. The use of the real part, $\text{Re}\{\cdot\}$, ensures that the image domain representation is real-valued, as expected for intensity images.

2.2. Algorithmic structure

The R2D2 algorithm proposes a paradigm shift in radio interferometry. It involves training a collection of I DNNs, denoted as $(\mathbf{N}_{\hat{\theta}^{(i)}})_{1 \leq i \leq I}$, each network defined by its learned parameters $(\hat{\theta}^{(i)} \in \mathbb{R}^Q)_{1 \leq i \leq I}$. Each DNN $\mathbf{N}_{\hat{\theta}^{(i)}}$ takes as input the previous image estimate $\mathbf{x}^{(i-1)}$ and its associated residual dirty image $\mathbf{r}^{(i-1)}$, defined as:

$$\mathbf{r}^{(i-1)} = \mathbf{x}_d - \kappa \text{Re}\{\Phi^\dagger \Phi\} \mathbf{x}^{(i-1)}. \quad (2)$$

The current image estimate is then updated as:

$$\mathbf{x}^{(i)} = [\mathbf{x}^{(i-1)} + \mathbf{N}_{\hat{\theta}^{(i)}}(\mathbf{r}^{(i-1)}, \mathbf{x}^{(i-1)})]_+, \quad (3)$$

where $[\cdot]_+$ denotes the projection of its argument into the non-negative orthant, ensuring the non-negativity of the reconstructed image, an essential physical constraint on intensity images. Here, each DNN $\mathbf{N}_{\hat{\theta}^{(i)}}$ learns to predict a residual image using the previous image estimate and its corresponding residual dirty image. The output residual image is added to the previous image estimate, effectively refining it. In other words, R2D2 can be understood as a learned version of CLEAN (Dabbech et al. 2024), with minor cycles encapsulated in a DNN model, trained specifically for each iteration. The final reconstruction corresponds to the I -th iteration i.e. $\hat{\mathbf{x}} = \mathbf{x}^{(I)}$. In the absence of the non-negativity constraint, R2D2’s reconstruction would take the simple series expression $\hat{\mathbf{x}} = \sum_{i=1}^I \mathbf{N}_{\hat{\theta}^{(i)}}(\mathbf{r}^{(i-1)}, \mathbf{x}^{(i-1)})$, which motivates the denomination of the ‘‘DNN series’’.

R2D2 DNNs are trained using supervised learning. Considering K training samples, for each iteration i , the goal is to minimise the error between the current image estimate $\mathbf{x}_k^{(i)}$ and the target ground-truth image \mathbf{x}_k^* for the k -th training sample. This is achieved using an ℓ_1 -norm loss function with a non-negativity constraint on

the target image:

$$\min_{\boldsymbol{\theta}^{(i)} \in \mathbb{R}^Q} \frac{1}{K} \sum_{k=1}^K \|\mathbf{x}_k^* - [\mathbf{x}_k^{(i-1)} + \mathbf{N}_{\boldsymbol{\theta}^{(i)}}(\mathbf{r}_k^{(i-1)}, \mathbf{x}_k^{(i-1)})]_+\|_1, \quad (4)$$

This loss ensures the DNN generates output residual images, promoting the non-negativity of the image estimate, while penalising large deviations from the ground truth. Loss functions of the form (4) are optimised using the Root Mean Square Propagation (RMSProp) algorithm, with the learnable parameters of each network initialised from the estimated parameters of the preceding network.

3. ROBUST R2D2

This section provides the details of the key advancements ensuring the robustness of R2D2, targeting the formation of 512×512 monochromatic intensity images under a VLA-specific observational setup. We focus on three core aspects: the training methodology that improves model generalisation, the introduction of a convergence criterion, and a novel DNN architecture underpinning the R2D2 series. For insights into the reliability and interpretability of the algorithm’s outputs, we present an ensemble averaging approach for epistemic uncertainty quantification.

3.1. Generalised training dataset

In building the training dataset, we followed closely the training setup described in Aghabiglou et al. (2024). The same diverse database of 512×512 ground-truth monochromatic intensity images was considered, derived from low-dynamic-range radio and optical astronomy images as well as medical imaging sources. In particular, high-dynamic-range ground-truth images were obtained by applying a pixel-wise exponentiation transform (Terris et al. 2022), with their dynamic range, denoted by a , randomly selected within the range $[10^3, 5 \times 10^5]$. Realistic RI data were simulated, combining VLA configurations A and C. Fourier sampling patterns were generated by uniformly randomising several parameters including (i) the pointing direction, (ii) the total observation durations with configurations A and C (denoted by $t_{\text{obs-A}}$ and $t_{\text{obs-C}}$, respectively), and (iii) the spectral specifications. These consist of the frequency bandwidth, described by the ratio of the highest to the lowest frequency (ρ_{freq}), and the number of observation frequencies combined for image formation (n_{freq}).

To enhance the robustness of R2D2 to varying observational conditions, the RI Fourier sampling is further diversified in this study by randomising the previously fixed integration time ($t_{\text{samp.}}$) in the set $\{4, 8, 16, 32\}$ seconds. The total number of points in the resulting Fourier

sampling patterns ranges from 2×10^5 to 27.2×10^6 , spanning a range approximately one order of magnitude wider than the previously considered patterns. Moreover, a multi-scan multi-noise setup was considered instead of a single-scan setup. In practice, the target radio source is often observed alongside other nearby calibrator sources with known flux densities. Data acquisition is therefore performed in time scans, alternating between the target source and the calibrator sources for the duration of the observation. The number of time scans (n_{scan}) was uniformly randomised between 1 and 8, with a lag time of up to 20% of the observation duration. Under these considerations, the standard deviation of the additive noise vector \mathbf{n} corrupting the simulated RI data \mathbf{y} varies per time scan and frequency channel. Let $s \in \{1, \dots, n_{\text{scan}}\}$ denote the index of a given time scan, and $f \in \{1, \dots, n_{\text{freq}}\}$ the index of a frequency channel. The standard deviation of the associated noise block $\mathbf{n}_{s,f}$ denoted by $\tau_{s,f}$ is set following a stipulation of Terris et al. (2022) linking the measurement noise to the dynamic range of the radio image of interest. Specifically, $\tau_{s,f} = a^{-1} \sqrt{2 \|\text{Re}\{\boldsymbol{\Phi}_{s,f}^\dagger \boldsymbol{\Phi}_{s,f}\}\|_S}$, where $\boldsymbol{\Phi}_{s,f}$ is the associated measurement operator block, and $\|\cdot\|_S$ denotes the spectral norm of its argument operator.

R2D2 robustness to varying imaging settings is also propelled by varying the previously fixed pixel resolution and visibility-weighting scheme adopted for the generation of the dirty images via back-projection. More precisely, Briggs weighting scheme (Briggs 1995), previously adopted with a fixed robustness parameter (ρ_{br}), was uniformly randomised in the range $[-1, 1]$, with lower values approaching uniform weighting, and higher values approaching natural weighting. The pixel resolution of the dirty images was also randomly chosen to reflect a super-resolution factor during imaging (ρ_{sr}) in the range $[1.5, 2.5]$. In the remainder of this article, we refer to the training setup of Aghabiglou et al. (2024) as \mathcal{T}_1 , and to the more generalised training setup proposed herein as \mathcal{T}_2 . A summary of the parameter space underlying both \mathcal{T}_1 and \mathcal{T}_2 is provided in Table 1.

3.2. Series convergence

The concept of convergence in the R2D2 paradigm is defined as the point at which the residual dirty image matches the noise level in ℓ_2 sense, indicating that further iterations will not yield any improvements in data fidelity. This serves as a critical criterion for both the training and image reconstruction steps, enabling higher computational efficiency while maintaining imaging precision.

In the sequential training of the R2D2 DNN series, convergence is evaluated for each training image pair

Table 1. Parameter choice of the training setup \mathcal{T}_1 described in Aghabiglou et al. (2024), and the proposed training setup \mathcal{T}_2 . Observational parameters include the pointing direction (the declination (DEC) and right ascension (RA)), the total observation time with VLA configurations A ($t_{\text{obs-A}}$) and C ($t_{\text{obs-C}}$), the sampling integration time $t_{\text{samp.}}$, the number of time scans (n_{scan}), the frequency bandwidth ratio (ρ_{freq}), the number of frequencies (n_{freq}), and the properties of the additive random Gaussian noise. Imaging parameters include the super-resolution factor (ρ_{sr}) determining the pixel resolution, and the robustness parameter of Briggs weighting (ρ_{br}). Values in $[\cdot, \cdot]$ indicate the lower and upper bounds for generating uniformly random parameter values.

Training setup	Observational parameters							Imaging parameters			
	DEC (degrees)	RA (J2000) (hr)	$t_{\text{obs-A}}$ (hr)	$t_{\text{obs-C}}$ (hr)	$t_{\text{samp.}}$ (sec.)	ρ_{freq}	n_{freq}	Noise variance	n_{scan}	ρ_{sr}	ρ_{br}
\mathcal{T}_1	[5, 60]	[0, 23]	[5, 10]	[1, 3]	36	[1, 2]	{1, ..., 4}	homogeneous	1	1.5	0
\mathcal{T}_2					{4, 8, 16, 32}			time-scan & frequency-dependent	{1, ..., 8}	[1.5, 2.5]	[-1, 1]

($\mathbf{x}_k^*, \mathbf{x}_{d_k}$) based on the evolution of the associated residual dirty image. More precisely, the inverse problem associated with the image pair is considered to be solved if, at a given iteration $i > 1$, the residual dirty image satisfies the condition $\|\mathbf{r}_k^{(i)}\|_2^2 \leq \|\kappa_k \text{Re}\{\mathbf{\Phi}_k^\dagger \mathbf{\Phi}_k\} \mathbf{n}_k\|_2^2$, where right-hand side represents the ℓ_2 -norm of the back-projected noise vector in the image-domain, assumed known during training. Once convergence is achieved, the image pair is removed from the training dataset utilised to streamline the training of subsequent DNNs. This approach reduces the size of the training dataset, while also ensuring that subsequent DNNs focus on the remaining, not yet solved, inverse problems.

In this study, we extend the pruning strategy to the validation dataset to prevent early stopping of training, caused by the convergence of the evaluation metrics over a static validation set. This pruning approach not only reduces computational costs by focusing on challenging inverse problems but also enhances the learning of the last terms of the DNN series.

In the image reconstruction step, the convergence criterion ensures that iterations stop when further improvements in reconstruction quality are unlikely. In practice, the exact noise level of the input dirty image is often unknown, prompting us to adopt alternative stopping conditions. Specifically, two stopping criteria are applied to indicate R2D2 convergence, and the process terminates when either condition is met. First, iterations are stopped if the ℓ_2 -norm of the relative difference between consecutive residual dirty images falls below 10^{-3} . This condition reflects that the changes in residual dirty images across iterations are no longer significant. Second, iterations are terminated if the data fidelity term increases for a second time during the process, as this could indicate that beyond a certain point, iterative updates driven by the model’s prior may produce solutions that are less data-consistent. These criteria ensure that R2D2 iterations stop when the residual dirty images are effectively compatible with noise, optimising computational efficiency while preserving imaging precision.

3.3. U-WDSR DNN architecture

In this section, we explore a novel DNN architecture in the R2D2 algorithm and analyse its impact on imaging precision and the computational efficiency. The advanced architecture, which we dub U-WDSR, combines the WDSR residual body architecture, originally proposed by Yu et al. (2018) for image and video super-resolution, with the U-Net architecture. More precisely, the WDSR residual body is incorporated into the U-Net architecture as a block interlaced with the conventional convolution layers of the same channel widths.

The U-WDSR architecture retains the primary structural components of U-Net, including the contracting and expanding paths, skip connections, and pooling/upsampling operations. For details regarding the previously adopted U-Net architecture, such as the arrangement of convolutional layers, pooling, and upsampling layers, we refer the reader to our earlier work (Aghabiglou et al. 2024).

The integrated WDSR residual body maintains an identical architecture to Yu et al. (2018), featuring an augmented number of blocks extended to 16. It incorporates several key features, including wide activation, dense connections, weight normalisation, and low-rank convolution, that collectively improve its imaging precision and computational efficiency. Firstly, each residual block in the WDSR body expands the number of channels prior to the ReLU activation layer. This wide activation approach allows for more information to flow through the network, enabling the model to capture more intricate and detailed patterns in the data. By widening the channels, the architecture achieves higher feature capacity without significantly increasing computational overhead. Secondly, dense connections enable feature reuse by reintroducing feature maps generated at earlier layers back into later layers. This design ensures that features learned at each layer are accessible multiple times, facilitating better gradient flow during training and promoting efficient learning. This repeated reuse of features allows the network to learn richer and more hierarchical representations of the data. Thirdly, weight

normalisation stabilises training by re-parametrising the weight vectors. This approach improves convergence and enables the network to achieve better performance, particularly in deep models. Finally, linear low-rank convolutions balance the computational cost introduced by wide activation, reducing the dimensionality of intermediate representations while retaining critical information. Both U-Net and U-WDSR architectures are illustrated in Fig. 1.

In the remainder of this paper, R2D2 models taking U-Net as the core DNN architecture (\mathcal{A}_1), and trained with the respective training setups \mathcal{T}_1 and \mathcal{T}_2 will be referred to as R2D2 $_{\mathcal{A}_1, \mathcal{T}_1}$ and R2D2 $_{\mathcal{A}_1, \mathcal{T}_2}$. Similarly, R2D2 models taking U-WDSR as the core architecture (\mathcal{A}_2) will be referred to as R2D2 $_{\mathcal{A}_2, \mathcal{T}_1}$ and R2D2 $_{\mathcal{A}_2, \mathcal{T}_2}$.

3.4. Epistemic uncertainty quantification

Uncertainty quantification is critical for ill-posed inverse problems. On the one hand, incomplete data introduces aleatoric uncertainty. On the other hand, epistemic uncertainty arises from the choice of regularisation models. Given the deterministic nature of R2D2, direct aleatoric uncertainty assessment is not feasible. In this section, we propose an ensemble averaging approach to quantify epistemic uncertainty and evaluate the robustness of R2D2 models from two perspectives. First, multiple series are trained with different random initialisations of the first DNN, capturing variability arising from the training process. Second, variations in visibility-weighting schemes introduced by different Briggs parameters ρ_{br} , also contribute to epistemic uncertainty.

To quantify uncertainty in both cases, we define a unified evaluation approach. Specifically, we consider the concatenation of reconstructed image estimates $\widehat{\mathbf{X}} \in \mathbb{R}^{N \times R}$, represented as:

$$\widehat{\mathbf{X}} = [\widehat{\mathbf{x}}_1, \dots, \widehat{\mathbf{x}}_R], \quad (5)$$

where $r \in \{1, \dots, R\}$ indexes the reconstructed images. For model-based epistemic uncertainty, $\widehat{\mathbf{X}}$ denotes the concatenation of reconstructed images resulting from different R2D2 realisations trained with distinct random initialisations. For epistemic uncertainty induced by visibility weighting, $\widehat{\mathbf{X}}$ comprises the concatenation of images reconstructed with different Briggs parameters ρ_{br} .

The pixel-wise mean image $\boldsymbol{\mu}(\widehat{\mathbf{X}}) \in \mathbb{R}^N$ is defined as:

$$\boldsymbol{\mu}(\widehat{\mathbf{X}}) = \frac{1}{R} \sum_{r=1}^R \widehat{\mathbf{x}}_r, \quad (6)$$

The relative uncertainty image, denoted as $[\boldsymbol{\sigma}/\boldsymbol{\mu}](\widehat{\mathbf{X}})$, represents the pixel-wise ratio of the standard deviation

to the mean and is given by:

$$[\boldsymbol{\sigma}/\boldsymbol{\mu}](\widehat{\mathbf{X}}) = \begin{cases} \frac{1}{\boldsymbol{\mu}(\widehat{\mathbf{X}})} \sqrt{\frac{\sum_1^R (\widehat{\mathbf{x}}_r - \boldsymbol{\mu}(\widehat{\mathbf{X}}))^2}{R}} & \text{if } \boldsymbol{\mu}(\widehat{\mathbf{X}}) > 1/\widehat{a}, \\ 0 & \text{otherwise,} \end{cases} \quad (7)$$

here, $\widehat{a} > 1$ represents the target dynamic range estimated as $\widehat{a}^{-1} = \tau/\sqrt{2\|\text{Re}\{\boldsymbol{\Phi}^\dagger \boldsymbol{\Phi}\}\|_S}$ (Terris et al. 2022). This formulation ensures that uncertainty is quantified only for non-zero pixels within the target dynamic range.

3.5. Training implementation & computational cost

The training of R2D2 models was conducted using the PyTorch library in Python (Paszke et al. 2019), leveraging the TorchKbNufft package (Muckley et al. 2020) for the implementation of the measurement operator model. TorchKbNufft provides an efficient and flexible NUFFT implementation, offering options for either fast table-based interpolation or exact computation using the sparse interpolation matrix. The former was considered for RI data simulation and the computation of the residual data during training.

Training was carried out on Cirrus, a UK Tier 2 high-performance computing (HPC) facility. The utilised GPU nodes consist of two 20-core Intel Xeon Gold 6148 processors, four NVIDIA Tesla V100-SXM2-16GB GPUs, and 384 GB of DRAM memory. The learning rate was fixed to 10^{-4} , and the batch size was set to 4 for R2D2 $_{\mathcal{A}_1, \mathcal{T}_2}$ and 1 for R2D2 $_{\mathcal{A}_2, \mathcal{T}_2}$, respectively, due to GPU memory limitations.

Under the proposed training setup \mathcal{T}_2 , we compare the training computational cost of the models R2D2 $_{\mathcal{A}_1, \mathcal{T}_2}$ and R2D2 $_{\mathcal{A}_2, \mathcal{T}_2}$, as well as the first DNN in their series as standalone end-to-end DNN models, namely U-Net, and U-WDSR, respectively. Table 2 summarises the key training details, including the number of iterations I . The reported total computational cost in GPU hours is obtained from averaging over $R = 5$ realisations of the R2D2 models.

With regards to end-to-end DNN models, the training computational cost of U-WDSR is nearly twice as high as that of U-Net, mainly due to the increased complexity of the former architecture. This trend is also observed in the training of the full DNN series underpinning their corresponding R2D2 models. Interestingly, the computational cost of updating residual dirty images is slightly lower for the U-WDSR-based R2D2 model, R2D2 $_{\mathcal{A}_2, \mathcal{T}_2}$, even though both trained the same number of DNNs. This is explained by the adopted data-pruning strategy combined with the efficiency of the advanced architecture U-WDSR. Fig. 2 illustrates the evolution of the training dataset size during training. R2D2 $_{\mathcal{A}_1, \mathcal{T}_2}$ reaches approximately 65% of its initial size by the final itera-

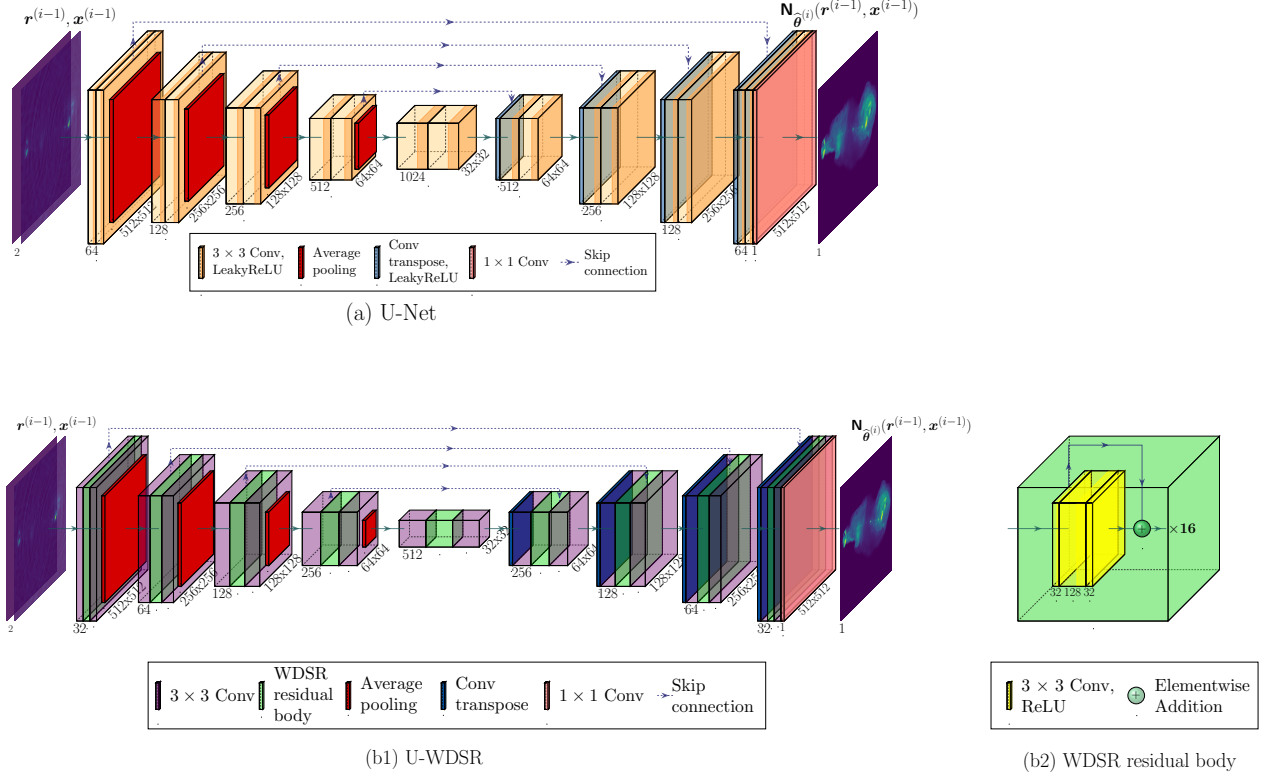


Figure 1. R2D2 core DNN architectures. The first row panel (a) illustrates the U-Net model architecture (Aghabiglou et al. 2024). The second row presents the U-WDSR model: panel (b1) shows the U-WDSR architecture and panel (b2) depicts its WDSR layer. The WDSR residual body (in green boxes) is interlaced with the convolutional layers of the U-Net. WDSR consists of 16 consecutive residual blocks. At each stage, the spatial size of feature maps is indicated at the lower centre of each box. The number of channels is indicated at the outer edge of each box.

Table 2. Training computation details of U-Net, U-WDSR, R2D2 $_{A_1, \mathcal{T}_2}$, and R2D2 $_{A_2, \mathcal{T}_2}$, all trained using the training setup \mathcal{T}_2 . The results are presented in terms of: the number of iterations (I), the number of learnable parameters in each network component (Q), and the total number of training epochs (n_{epochs}). The total computational cost is measured in GPU hours ($t_{\text{tot.}}$), broken down into the cost spent updating residual dirty images ($t_{\text{dat.}}$) and the cost used for DNN training and updating image estimates ($t_{\text{tra.}}$).

Algorithm	I	$Q(\times 10^6)$	n_{epochs}	n_{GPU}	GPU hr		
					$t_{\text{tot.}}$	$t_{\text{dat.}}$	$t_{\text{tra.}}$
U-Net	1	31	174	4	85.6	4.4	81.2
U-WDSR	1	20.9	55	4	165.7	4.4	161.3
R2D2 $_{A_1, \mathcal{T}_2}$	25	31	325	4	231.6	85.5	146.1
R2D2 $_{A_2, \mathcal{T}_2}$	25	20.9	142	4	420.9	72.6	348.3

tion. In contrast, R2D2 $_{A_2, \mathcal{T}_2}$ exhibits a steeper decline in dataset size, converging to around 40% of the original dataset by the last iteration. This indicates faster convergence enabled by the advanced architecture U-WDSR.

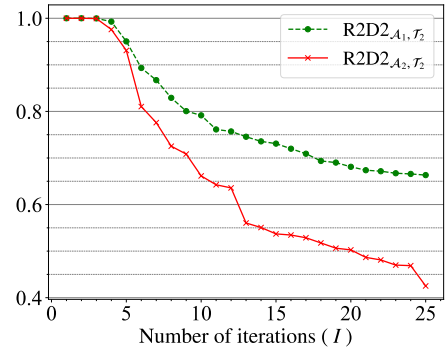


Figure 2. Evolution of the size of the training dataset throughout the iterations of R2D2 $_{A_1, \mathcal{T}_2}$ and R2D2 $_{A_2, \mathcal{T}_2}$, shown as a fraction of the size of the initial training dataset.

4. SIMULATION AND RESULTS

This section presents a comprehensive evaluation of R2D2, focusing on its robust performance in terms of reconstruction quality and computational efficiency under various experimental setups, using VLA-specific observational settings for the formation of 512×512

monochromatic intensity images. The evaluation is structured into four distinct studies. The first study compares the performance of the proposed R2D2 models to the early version. The second study benchmarks R2D2 against state-of-the-art RI algorithms. The third study quantifies R2D2’s epistemic uncertainty across its realisations. The fourth study investigates R2D2’s epistemic uncertainty under varying visibility-weighting schemes to evaluate the adaptability of R2D2 to diverse imaging conditions.

Ground-truth images used for the test dataset were derived from four real radio images, namely the giant radio galaxies 3c353 (sourced from the NRAO Archives) and Messier 106 (Shimwell et al. 2022), and the radio galaxy clusters Abell 2034 and PSZ2 G165.68+44.01 (Botteon et al. 2022). Details on the pre-processing involved can be found in Aghabiglou et al. (2024).

4.1. Benchmark algorithms & parameter choice

R2D2 performance is studied against the RI imaging algorithms uSARA and AIRI in BASPLib, and multi-scale CLEAN (Cornwell 2008) in the WSClean software (Offringa et al. 2014; Offringa & Smirnov 2017). R2D2, AIRI, and uSARA benefit from GPU-accelerated Python implementations. Their core operations, including data fidelity, regularisation steps for uSARA, denoising steps for AIRI, and R2D2 DNNs image reconstruction, are implemented using PyTorch. BASPLib provides four options for implementing the RI measurement operator model. Three of these consist in different implementations of the NUFFT including TorchKbNufft (Muckley et al. 2020), FINUFFT (Shih et al. 2021), and PyNUFFT (Lin 2018). The fourth option leverages the PSF, which under the assumption of a narrow field of view, enables approximating the RI mapping operator $\Phi^\dagger \Phi$ via a convolution with the PSF. This approach can benefit algorithms like R2D2, AIRI, and uSARA, whose iteration rules call explicitly for the dirty image and the mapping operator $\Phi^\dagger \Phi$ to update the residual dirty image. R2D2, uSARA and AIRI were deployed on a single GPU. As for WSClean, the software is not optimised for small-scale imaging on GPU. Therefore, it was deployed on a single CPU. Under these considerations, direct comparison of its computational performance with the GPU-accelerated algorithms is inherently unfair.

Conceptually, uSARA, AIRI and CLEAN involve free parameters which must be carefully selected. More specifically, uSARA features a parameter balancing its handcrafted regularisation against data fidelity. AIRI involves a parameter controlling the choice of the DNN denoiser and the adjustment of its input to the training noise level via a scaling operation. uSARA and

AIRI parameter selection is automated using noise-driven heuristics (Terris et al. 2022; Dabbech et al. 2022; Wilber et al. 2023). Yet, optimal results often require some tweaking around the heuristic values. In fact, in all experiments, uSARA parameter was set to twice the heuristic value. AIRI parameter was set at the heuristic for all RI data, except those simulated using ground-truth images derived from 3c353, where 3 times the heuristic value was considered. As for WSClean, multi-scale CLEAN parameters are often set to the default nominal values. However, some adjustments might be required for optimal results. In all experiments, auto-masking and threshold parameters of CLEAN were set to 2.0 and 0.5 times the estimated noise level, respectively. In contrast, R2D2 is independent of such fine-tuning requirements and is free of regularisation parameters. This independence highlights a significant advantage of R2D2, enabling robust performance without the need for manual adjustments, unlike the benchmark algorithms.

4.2. Evaluation metrics

The reconstruction quality achieved by all algorithms is analysed through both qualitative and quantitative assessments, whereby (i) image estimates and associated residual dirty images are inspected visually, (ii) fidelity to the ground truth is evaluated using the signal-to-noise ratio (SNR) metric, computed in linear scale and logarithmic scale (logSNR), (iii) data fidelity is evaluated using the residual-to-dirty image ratio (RDR) metric, and (iv) relative uncertainty images are assessed using the mean relative uncertainty (MRU) metric, defined below.

The SNR measures the overall quality of the reconstructed image by comparing the estimate $\hat{\mathbf{x}}$ to the ground truth \mathbf{x}^* , and is defined as:

$$\text{SNR}(\hat{\mathbf{x}}, \mathbf{x}^*) = 20 \log_{10} \left(\frac{\|\mathbf{x}^*\|_2}{\|\mathbf{x}^* - \hat{\mathbf{x}}\|_2} \right). \quad (8)$$

In high dynamic range scenarios, the logSNR metric provides a more sensitive metric for faint structures and low-intensity regions. To compute it, we first apply a logarithmic transformation to the images involved, parametrised by the target dynamic range a , and defined as:

$$\text{rlog}(\mathbf{x}) = x_{\max} \log_a \left(\frac{a}{x_{\max}} \mathbf{x} + \mathbf{1} \right), \quad (9)$$

where x_{\max} is the peak pixel value of the image \mathbf{x} , and $\mathbf{1} \in \mathbb{R}^N$ is a vector of ones. By setting a to the dynamic range of the ground truth, the logSNR is computed as:

$$\log\text{SNR}(\hat{\mathbf{x}}, \mathbf{x}^*) = \text{SNR}(\text{rlog}(\hat{\mathbf{x}}), \text{rlog}(\mathbf{x}^*)). \quad (10)$$

Data fidelity is evaluated by comparing the estimated residual dirty image $\widehat{\mathbf{r}}$ to the dirty image \mathbf{x}_d . We consider the image-domain data fidelity metric, RDR, defined as:

$$\text{RDR}(\widehat{\mathbf{r}}, \mathbf{x}_d) = \frac{\|\widehat{\mathbf{r}}\|_2}{\|\mathbf{x}_d\|_2}. \quad (11)$$

A lower value of RDR indicates higher data fidelity in the image domain.

We evaluate R2D2’s robustness by examining its pixel-wise relative uncertainty images $[\boldsymbol{\sigma}/\boldsymbol{\mu}](\widehat{\mathbf{X}})$, obtained as per (7) and report the corresponding mean relative uncertainty value denoted by MRU which reads:

$$\text{MRU}(\widehat{\mathbf{X}}) = \frac{1}{N} \sum_{n=1}^N \left([\boldsymbol{\sigma}/\boldsymbol{\mu}](\widehat{\mathbf{X}}) \right)_n. \quad (12)$$

This metric encapsulates the overall epistemic uncertainty of R2D2 models, offering insights into their stability and reliability across different R2D2 realisations and variations in ρ_{br} throughout its iterations.

We also evaluate the computational performance of the imaging algorithms. This includes measuring the total number of iterations I , the total computational time $t_{\text{tot.}}$, and the average computational time per iteration for the data fidelity step $t_{\text{dat.}}$ and the regularisation step $t_{\text{reg.}}$. Since R2D2, AIRI, and uSARA were deployed on a single GPU, their computational time is reported in seconds. The same applies to WSClean, which was run on a single CPU.

4.3. Robust R2D2 vs. early version

In this study, we assess the robustness of the proposed models in comparison with the earlier model from Aghabiglou et al. (2024). In particular, we investigate the impact of (i) the choice of the core DNN architecture and (ii) the design of the training setup. Two experimental setups were considered. The first experimental setup, dubbed \mathcal{E}_1 , corresponds to the test dataset adopted in Aghabiglou et al. (2024, Table 2), that is consistent with the training setup \mathcal{T}_1 . The second experimental setup, dubbed \mathcal{E}_2 , is fully generalised with all observational and imaging parameters uniformly randomised following the proposed training setup \mathcal{T}_2 . Specifically, \mathcal{E}_2 is composed of 200 inverse problems, simulated from 50 ground-truth images of varying dynamic range for each of the four source radio images.

Reconstruction results in terms of SNR and logSNR metrics, presented in Table 3, demonstrate that R2D2 models underpinned by the advanced U-WDSR architecture (R2D2 $_{\mathcal{A}_2, \mathcal{T}_1}$, R2D2 $_{\mathcal{A}_2, \mathcal{T}_2}$) consistently outperform the ones underpinned by U-Net (R2D2 $_{\mathcal{A}_1, \mathcal{T}_1}$, R2D2 $_{\mathcal{A}_1, \mathcal{T}_2}$) in both experimental setups \mathcal{E}_1 and \mathcal{E}_2 . When tested on \mathcal{E}_2 , R2D2 $_{\mathcal{A}_2, \mathcal{T}_1}$ trained with fixed imaging settings still

Table 3. Performance of the different R2D2 models under different experimental setups. Specifically, we compare the reconstruction quality (SNR and logSNR) achieved by the proposed models R2D2 $_{\mathcal{A}_1, \mathcal{T}_2}$ and R2D2 $_{\mathcal{A}_2, \mathcal{T}_2}$ against the earlier model R2D2 $_{\mathcal{A}_1, \mathcal{T}_1}$ (Aghabiglou et al. 2024). We also provide the results of the model R2D2 $_{\mathcal{A}_2, \mathcal{T}_1}$. The considered experimental setups \mathcal{E}_1 and \mathcal{E}_2 are consistent with the respective training setups \mathcal{T}_1 and \mathcal{T}_2 . All reported values represent mean \pm standard deviation, calculated over 200 inverse problems.

R2D2 model	Tested on	SNR (dB)	logSNR (dB)
R2D2 $_{\mathcal{A}_1, \mathcal{T}_1}$	\mathcal{E}_1	33.7 \pm 1.5	25.1 \pm 4.9
R2D2 $_{\mathcal{A}_1, \mathcal{T}_2}$		33.2 \pm 2.3	24.4 \pm 5.3
R2D2 $_{\mathcal{A}_2, \mathcal{T}_1}$		34.7 \pm 1.6	25.7 \pm 4.9
R2D2 $_{\mathcal{A}_2, \mathcal{T}_2}$		34.3 \pm 1.6	25.6 \pm 4.8
R2D2 $_{\mathcal{A}_1, \mathcal{T}_1}$	\mathcal{E}_2	20.2 \pm 12.0	12.4 \pm 12.2
R2D2 $_{\mathcal{A}_1, \mathcal{T}_2}$		30.0 \pm 3.0	23.4 \pm 4.2
R2D2 $_{\mathcal{A}_2, \mathcal{T}_1}$		28.6 \pm 4.7	21.5 \pm 5.6
R2D2 $_{\mathcal{A}_2, \mathcal{T}_2}$		31.2 \pm 2.4	24.6 \pm 4.2

performed reliably, as opposed to R2D2 $_{\mathcal{A}_1, \mathcal{T}_1}$. This highlights the robustness of the R2D2 model underpinned by the novel architecture U-WDSR and its ability to generalise beyond its training setup. When tested on \mathcal{E}_1 , both R2D2 $_{\mathcal{A}_1, \mathcal{T}_2}$ and R2D2 $_{\mathcal{A}_2, \mathcal{T}_2}$, trained under a generalised setup, achieve a comparable performance to those trained under the more specific setup of \mathcal{E}_1 . These findings showcase that generalising the training setup through stochastic variations in all observational and imaging settings does not lead to suboptimal results compared to testing in a more specific setup. Moreover, they emphasise that the combination of an advanced DNN architecture, such as U-WDSR, and a diverse, well-constructed training setup significantly boosts the robustness of the R2D2 model.

4.4. Robust R2D2 vs. benchmarking algorithms

We study the performance of the proposed R2D2 models in comparison with the benchmarking algorithms using the experimental setup \mathcal{E}_2 introduced in Section 4.3. Numerical results of all algorithms are summarised in Table 4, which includes the reconstruction quality metrics as well as additional computational metrics. Reported values are computed as averages across all inverse problems. Additionally, results of all iterative algorithms, with the exception of CLEAN, are reported for the four different implementations of the RI mapping operator $\Phi^\dagger \Phi$, presented in Section 4.1.

Table 4. Evaluation of the performance of the proposed R2D2 models against benchmarking RI algorithms. Reconstruction quality metrics are SNR, logSNR, and RDR. Computational performance is evaluated using the total number of iterations (I), the total reconstruction time ($t_{\text{tot.}}$), the average time per iteration for both the data fidelity step ($t_{\text{dat.}}$) and the regularisation step ($t_{\text{reg.}}$). $[\Phi^\dagger\Phi]_{\text{imp.}}$ is indicating the measurement operator implementation. All reported values represent mean \pm standard deviation, calculated over 200 inverse problems.

Algorithm	SNR (dB)	logSNR (dB)	RDR ($\times 10^{-3}$)	I	$t_{\text{tot.}}$ (s)	$t_{\text{dat.}}$ (s)	$t_{\text{reg.}}$ (s)	$[\Phi^\dagger\Phi]_{\text{imp.}}$
CLEAN	12.0 ± 19.3	9.4 ± 18.9	3.29 ± 28.2	8.4 ± 1.0	106.5 ± 81.6	11.36 ± 9.76	1.38 ± 0.50	-
uSARA	28.1 ± 3.4	20.4 ± 3.4	2.15 ± 27.5	1482.2 ± 586.1	368.8 ± 296.8	0.1660 ± 0.1621	0.0806 ± 0.0646	TorchKbNufft
								PyNUFFT
								FINUFFT
								PSF
AIRI	28.3 ± 3.1	21.1 ± 3.8	2.24 ± 28.0	5000.0 ± 0.0	937.4 ± 801.8	0.1660 ± 0.1604	0.0016 ± 0.0584	TorchKbNufft
		21.0 ± 3.8						PyNUFFT
		157.0 ± 36.92						FINUFFT
		114.2 ± 3.450						PSF
U-Net	17.9 ± 3.0	6.8 ± 3.9	113.3 ± 589.2	1	0.641 ± 0.110	-	0.641 ± 0.110	-
U-WDSR	16.0 ± 3.6	6.6 ± 3.8	155.8 ± 815.5	1	0.662 ± 0.031	-	0.662 ± 0.031	-
R2D2 $_{\mathcal{A}_1, \mathcal{T}_2}$	30.0 ± 3.0	23.4 ± 4.2	4.07 ± 91.6	18.3 ± 5.6	7.243 ± 4.131	0.2123 ± 0.1932	0.0462 ± 0.4572	TorchKbNufft
					6.932 ± 3.960	0.1992 ± 0.1791	0.0197 ± 0.0686	PyNUFFT
					3.771 ± 1.224	0.0356 ± 0.0685	0.0212 ± 0.1104	FINUFFT
					3.342 ± 0.931	0.0003 ± 0.0001	0.0200 ± 0.0773	PSF
R2D2 $_{\mathcal{A}_2, \mathcal{T}_2}$	31.2 ± 2.4	24.6 ± 4.2	2.22 ± 28.1	15.8 ± 5.5	8.831 ± 3.923	0.2700 ± 0.1944	0.1059 ± 0.3221	TorchKbNufft
					9.023 ± 4.112	0.2437 ± 0.1756	0.0922 ± 0.1239	PyNUFFT
					5.951 ± 2.199	0.0867 ± 0.0854	0.0878 ± 0.1055	FINUFFT
					5.649 ± 1.911	0.0003 ± 0.0002	0.0862 ± 0.0871	PSF

NOTE—For CLEAN, the reported number of iterations corresponds to the number of major cycles required for convergence. Additionally, CLEAN diverged in three test inverse problems. These cases are therefore excluded from the reported results.

In terms of SNR and logSNR metrics, the results demonstrate that CLEAN and end-to-end DNN architectures (U-Net and U-WDSR) perform suboptimally. The benchmark algorithms uSARA and AIRI deliver comparable values, with the latter achieving marginally higher values. Interestingly, R2D2 models enable superior reconstruction quality, outperforming both uSARA and AIRI by almost 2 to 4 dB in both metrics. Focusing on R2D2 models, R2D2 $_{\mathcal{A}_2, \mathcal{T}_2}$ yields better reconstruction results than R2D2 $_{\mathcal{A}_1, \mathcal{T}_2}$, as per the findings of Section 4.3. When examining data fidelity via the metric RDR, one can see that R2D2 $_{\mathcal{A}_2, \mathcal{T}_2}$, AIRI, and uSARA are the best-performing algorithms, exhibiting comparable low values. In contrast, CLEAN delivers nearly 50% higher values, whereas R2D2 $_{\mathcal{A}_1, \mathcal{T}_2}$ obtains twice as high values, on average. Finally, both end-to-end DNNs perform poorly, confirming once again the advantage of the DNN series.

With regards to the different implementations of the RI mapping operator $\Phi^\dagger\Phi$, R2D2, AIRI, and uSARA maintain a consistent reconstruction quality in terms of SNR and logSNR with a relative difference of the order of 10^{-4} on average. This is somewhat expected in the context of narrow-field small-scale imaging. However, the different implementations of $\Phi^\dagger\Phi$ had a significant impact on the computational efficiency of the

different algorithms. Approximating the mapping operator using the PSF enabled the fastest computations of the residual dirty images (involved in the data fidelity step of the algorithms’ iterative structure). The NUFFT packages exhibited varying performance, with FINUFFT being the most efficient, and TorchKbNufft the slowest of the three. Generally, both FINUFFT and the PSF-based approximation yield comparable reconstruction times for the different algorithms, whereas PyNUFFT and TorchKbNufft yield 2 to 6 times slower reconstructions depending on the iterative nature of the RI algorithms. While highly efficient when conducted on GPU, it is important to note that the PSF approximation can severely hamper imaging precision, particularly in wide-field imaging where the so-called u -effect emanating from the non-coplanarity of the radio array becomes non-negligible, or more generally, in the presence of direction-dependent effects.

In terms of computational efficiency, R2D2 models enable fast reconstructions, taking few seconds only, thanks to the combination of their limited number of iterations (hence, a few passes through the data), and the inference speed of their DNNs. This constitutes a drastic reduction in reconstruction time compared to AIRI and uSARA, both taking several minutes to converge. Despite AIRI’s efficient denoising steps, its larger iter-

ation count results in longer total reconstruction times compared to uSARA. Nonetheless, thanks to their GPU implementations, both algorithms have significantly improved computational efficiency, with uSARA and AIRI being approximately 40 and 22 times faster than their CPU-based counterparts (Aghabiglou et al. 2024), respectively. R2D2 models are also faster than CLEAN. However, one must acknowledge that the considered implementation of CLEAN was not optimised for small-scale imaging on GPUs. Finally, both end-to-end DNN models, U-WDSR and U-Net, show an increased inference time, compared to the average execution time of DNN inference within the R2D2 series. This stems from the computational overhead incurred during DNN loading.

4.5. Uncertainty quantification via model realisations

We study the epistemic uncertainty of the proposed R2D2 models via ensemble averaging across different R2D2 realisations. To this aim, we trained $R = 5$ realisations for each of the models $\text{R2D2}_{\mathcal{A}_1, \mathcal{T}_2}$ and $\text{R2D2}_{\mathcal{A}_2, \mathcal{T}_2}$, and tested them on the experimental setup \mathcal{E}_2 described in Section 4.4. With $\widehat{\mathbf{X}}$ computed as per (5) from the resulting reconstruction vectors, we analyse the pixel-wise mean image $\boldsymbol{\mu}(\widehat{\mathbf{X}})$, and the pixel-wise relative uncertainty image $[\boldsymbol{\sigma}/\boldsymbol{\mu}](\widehat{\mathbf{X}})$. We also analyse the iteration-specific images $\boldsymbol{\mu}(\widehat{\mathbf{X}}^{(i)})$ and $[\boldsymbol{\sigma}/\boldsymbol{\mu}](\widehat{\mathbf{X}}^{(i)})$ for insights on the evolution of the epistemic uncertainty across the iterations of R2D2 models.

The first row of Fig. 3 investigates the epistemic uncertainty across R2D2 realisations by tracking its evolution over the metrics. Specifically, it presents (i) the reconstruction quality metrics, SNR and logSNR, of mean images $\boldsymbol{\mu}(\widehat{\mathbf{X}})$, and (ii) the mean value of the relative uncertainty image $[\boldsymbol{\sigma}/\boldsymbol{\mu}](\widehat{\mathbf{X}})$ denoted by MRU. For both R2D2 models, the mean images $\boldsymbol{\mu}(\widehat{\mathbf{X}})$ enable an incremental increase of both SNR and logSNR with respect to those obtained from the corresponding individual realisations. The examination of MRU reveals that although $\text{R2D2}_{\mathcal{A}_2, \mathcal{T}_2}$ exhibits higher initial uncertainty, it decreases more rapidly over iterations, ultimately achieving lower uncertainty values with a standard deviation (*i.e.* shaded area) that is 2.5 times lower than that of $\text{R2D2}_{\mathcal{A}_1, \mathcal{T}_2}$. This trend highlights the superior robustness of $\text{R2D2}_{\mathcal{A}_2, \mathcal{T}_2}$, achieving greater consistency in its image reconstruction as the number of iterations increases.

Panel (a) of Fig. 4 displays the reconstruction results of a selected inverse problem simulated using the image of the radio galaxy Messier 106. This figure includes ground truth, the dirty image, the estimated images of the worst and best realisations of $\text{R2D2}_{\mathcal{A}_1, \mathcal{T}_2}$ and

$\text{R2D2}_{\mathcal{A}_2, \mathcal{T}_2}$. It also provides their corresponding residual dirty images and relative uncertainty images $[\boldsymbol{\sigma}/\boldsymbol{\mu}](\widehat{\mathbf{X}})$. Showcasing the worst and best realisations only is motivated by the high visual consistency observed across all individual reconstructions of both $\text{R2D2}_{\mathcal{A}_1, \mathcal{T}_2}$ and $\text{R2D2}_{\mathcal{A}_2, \mathcal{T}_2}$. Even the worst-case reconstructions remain visually comparable to both the best realisations and mean images, illustrating the consistency across different model initialisations. Additionally, quantitative evaluation metrics confirm the superior performance of $\text{R2D2}_{\mathcal{A}_2, \mathcal{T}_2}$ compared to $\text{R2D2}_{\mathcal{A}_1, \mathcal{T}_2}$, which is in agreement with the findings of Section 4.4. The inspection of the residual dirty images reveals that $\text{R2D2}_{\mathcal{A}_1, \mathcal{T}_2}$ consistently exhibits discernible structures around the pixel positions of the brightest emission as well as ringing artefacts. However, these structures are less pronounced in the images obtained by $\text{R2D2}_{\mathcal{A}_2, \mathcal{T}_2}$. Examination of the relative uncertainty images $[\boldsymbol{\sigma}/\boldsymbol{\mu}](\widehat{\mathbf{X}})$ shows reduced uncertainty enabled by $\text{R2D2}_{\mathcal{A}_2, \mathcal{T}_2}$. These findings highlight the enhanced robustness and precision of $\text{R2D2}_{\mathcal{A}_2, \mathcal{T}_2}$ over $\text{R2D2}_{\mathcal{A}_1, \mathcal{T}_2}$.

4.6. Uncertainty quantification via visibility weighting

In this study, we evaluate the epistemic uncertainty quantification of the proposed R2D2 models by performing ensemble averaging over reconstructions obtained with different values of Briggs parameter ρ_{br} . We introduce the experimental setup \mathcal{E}_3 , comprising 1000 inverse problems with ground-truth images obtained from the image of 3c353, with varying dynamic ranges and observational settings consistent with the training setting described in Section 3.1. This transition from \mathcal{E}_2 (which consisted of 200 inverse problems) was necessary, as the smaller experimental setup led to instability in the results. Increasing the number of inverse problems ensures a more comprehensive and reliable evaluation. For each inverse problem, we generate five dirty images by back-projecting the simulated RI data to the image domain using Briggs weighting and considering different values of the Briggs parameter $\rho_{\text{br}} \in \{1, 0.5, 0, -0.5, -1\}$.

The second row of Fig. 3 examines the epistemic uncertainty introduced by varying the ρ_{br} . It tracks the evolution of the reconstruction quality metrics SNR and logSNR, and the uncertainty evaluation metric MRU throughout the iterations. At each iteration, mean images are computed by averaging over the 1000 inverse problems. In contrast, the metrics for $\widehat{\boldsymbol{x}}_{\text{R2D2}_{\mathcal{A}_1, \mathcal{T}_2}}$ and $\widehat{\boldsymbol{x}}_{\text{R2D2}_{\mathcal{A}_2, \mathcal{T}_2}}$ are averaged across all 5000 inverse problems, encompassing all chosen values of ρ_{br} . Consistent with the behaviour observed in Section 4.5, the mean images $\boldsymbol{\mu}(\widehat{\mathbf{X}})$ for both R2D2 models show a slight improvement in both SNR and logSNR compared to those

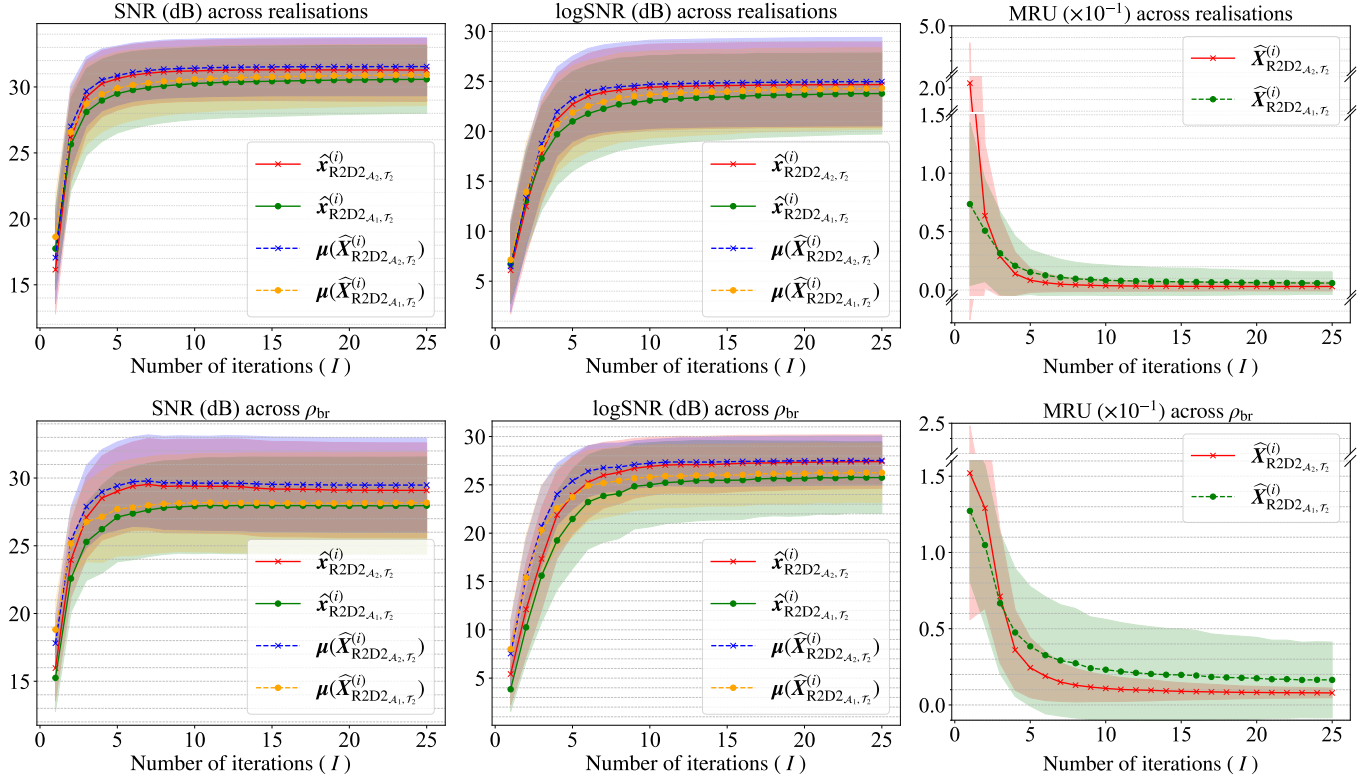


Figure 3. Analysis of R2D2’s epistemic uncertainty across R2D2 realisations (first row) and ρ_{br} variation (second row). From left to right: evolution of the reconstruction metrics SNR and logSNR, as well as the mean of the relative uncertainty image MRU, across the iterations of R2D2 models. The shaded area presents the standard deviations at each point.

obtained from the corresponding individual reconstructions. Furthermore, the metric MRU indicates a higher initial uncertainty for R2D2 $_{\mathcal{A}_2, \mathcal{T}_2}$ across variations in ρ_{br} but ultimately converges to a more robust result compared to R2D2 $_{\mathcal{A}_1, \mathcal{T}_2}$. Specifically, at convergence, R2D2 $_{\mathcal{A}_2, \mathcal{T}_2}$ achieves approximately 8 times lower standard deviation for MRU. This trend underscores the superior robustness of R2D2 $_{\mathcal{A}_2, \mathcal{T}_2}$ in handling variations in visibility weighting.

Panel (b) of Fig. 4 presents the reconstructed images obtained by R2D2 $_{\mathcal{A}_1, \mathcal{T}_2}$ and R2D2 $_{\mathcal{A}_2, \mathcal{T}_2}$, from the dirty images created with $\rho_{\text{br}} = 1$ and $\rho_{\text{br}} = -1$ values for a selected RI simulation using the radio image 3c353. The figure includes the ground truth, the dirty image for $\rho_{\text{br}} = 1$, and reconstructed images of R2D2 $_{\mathcal{A}_1, \mathcal{T}_2}$ and R2D2 $_{\mathcal{A}_2, \mathcal{T}_2}$. It also presents their corresponding residual dirty images and relative uncertainty images $[\sigma/\mu](\widehat{\mathbf{X}})$. Showcasing the results of the cases $\rho_{\text{br}} = -1$ and $\rho_{\text{br}} = 1$ is motivated by the observed consistency in reconstruction quality across all Briggs parameter values. These extremes represent uniform and natural weighting, effectively capturing the model’s robustness to visibility weighting variations. One can observe that the reconstructed images and mean image remain visually consistent across different ρ_{br} values for

both R2D2 models. The residual dirty images show discernible structures, particularly in the case of natural weighting ($\rho_{\text{br}} = 1$), which suggests that visibility weighting has a more noticeable impact on the fidelity to the dirty images than on the reconstructions themselves. Specifically, the residual dirty images of R2D2 $_{\mathcal{A}_1, \mathcal{T}_2}$ exhibit ringing artefacts for $\rho_{\text{br}} = 1$, which are absent in the corresponding residual dirty images of R2D2 $_{\mathcal{A}_2, \mathcal{T}_2}$. The relative uncertainty images show comparable behaviour for both R2D2 models across all ρ_{br} variations, further confirming that the models deliver stable reconstructions despite changes in visibility weighting.

Fig. 5 provides a comprehensive quantitative analysis of the metric variations across different ρ_{br} values. It depicts average values of SNR and logSNR values of R2D2 reconstructions as a function of Briggs parameter ρ_{br} . R2D2 $_{\mathcal{A}_1, \mathcal{T}_2}$ and R2D2 $_{\mathcal{A}_2, \mathcal{T}_2}$ achieve their best image quality in terms of SNR at $\rho_{\text{br}} = 0$, corroborating the fact that a balance between natural and uniform weighting often yields the highest reconstruction quality. In contrast, for logSNR, R2D2 $_{\mathcal{A}_2, \mathcal{T}_2}$ achieves its peak value at $\rho_{\text{br}} = 1$, whereas R2D2 $_{\mathcal{A}_1, \mathcal{T}_2}$ performs best at $\rho_{\text{br}} = 0$. This suggests that R2D2 $_{\mathcal{A}_2, \mathcal{T}_2}$ is more faithful to the standard expectation that natural weighting

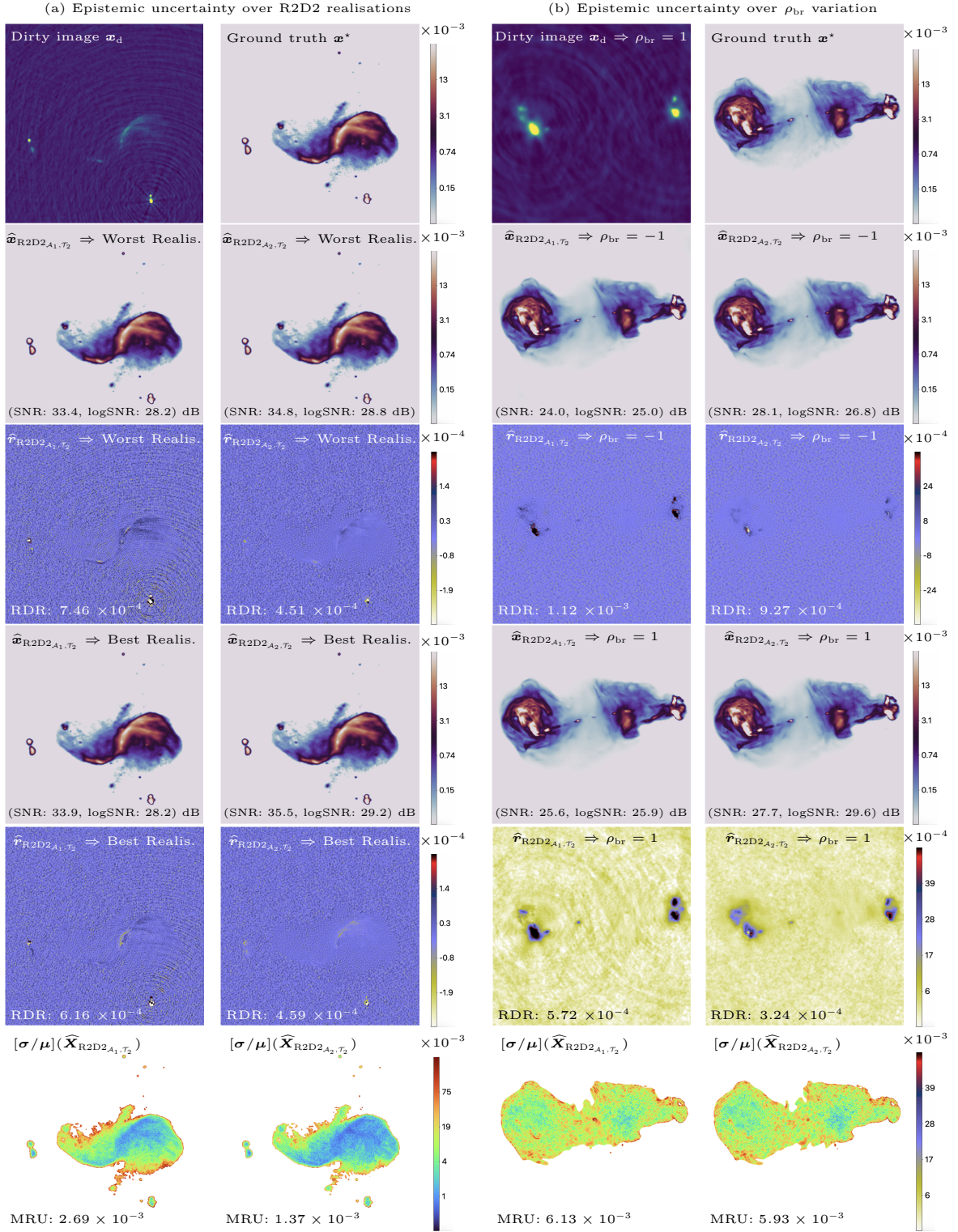


Figure 4. Illustration of R2D2's joint image estimation and uncertainty quantification functionality on selected RI simulations. Panel (a) focuses on epistemic uncertainty across R2D2 realisations utilising an image of Messier 106. Panel (b) focuses on epistemic uncertainty across variations of the parameter of Briggs weighting (ρ_{br}) utilising an image of 3c353. The first row in both panels displays the dirty image (left) and ground-truth image (right). In Panel (a) (resp. panel (b)), second and fourth rows show the respective estimated images for worst and best realisations of R2D2 $_{A_1, T_2}$ (left) and R2D2 $_{A_2, T_2}$ (right) (resp. estimated images with $\rho_{br} = -1$ and $\rho_{br} = 1$). Third and fifth rows in both panels show the corresponding residual dirty images. The sixth row displays the relative uncertainty image $[\sigma/\mu](\hat{\mathfrak{X}})$. Metrics are reported inside the associated images.

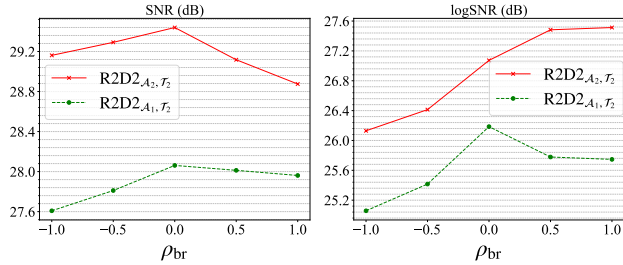


Figure 5. Reconstruction results of R2D2 models in terms of SNR (left) and logSNR (right) shown as functions of Briggs parameter ρ_{br} . Each point represents the average metric calculated over 1000 inverse problems corresponding to a specific ρ_{br} value.

maintains optimal sensitivity and thus delivers higher dynamic range.

5. REAL DATA AND RESULTS

In this section, we revisit VLA observations of the celebrated radio galaxy Cygnus A. These data have been heavily scrutinised in recent works (*e.g.* Dabbech et al. 2021; Arras et al. 2021; Roth et al. 2023) and most recently with the first incarnation of the R2D2 paradigm (Dabbech et al. 2024), where full observational details can be found. We first highlight the impact of the generalised training set by comparing the performance of the new models R2D2_{A₁, T₂} and R2D2_{A₂, T₂} with the early model R2D2_{A₁, T₁}. We further analyse the performance of the new models to showcase the impact of the core DNN architecture U-WDSR on the image reconstruction quality. For a fair comparison with the early model R2D2_{A₁, T₁}, we adhered to the imaging settings of its training setup \mathcal{T}_1 . We therefore formed images of size $N = 512 \times 512$ with a pixel resolution corresponding to $\rho_{sr} = 1.5$ using Briggs-weighted data with $\rho_{br} = 0$. Under the convergence criterion defined in Section 3.2, R2D2_{A₁, T₁}, R2D2_{A₁, T₂}, and R2D2_{A₂, T₂} called for 12, 16, and 15 iterations, respectively. To further investigate the proposed models' robustness, we examine epistemic uncertainty arising from R2D2 realisations and variations of visibility weighting during imaging. To this aim, we generated $R = 25$ reconstructions by combining all five model realisations (studied in Section 4.5) and applying five different visibility weights during imaging through variations of the value of the Briggs parameter ρ_{br} (studied in Section 4.6). Under this consideration, mean images are obtained by taking the pixel-wise mean of these 25 reconstructions.

Reconstruction results are displayed in Fig. 6. These include Cygnus A reconstructions and associated residual dirty images obtained from selected realisations of R2D2_{A₁, T₁}, R2D2_{A₁, T₂}, and R2D2_{A₂, T₂}. Mean im-

ages $\mu(\widehat{\mathbf{X}})$ and associated relative uncertainty images $[\sigma/\mu](\widehat{\mathbf{X}})$ obtained with R2D2_{A₁, T₂} and R2D2_{A₂, T₂} are also provided. For enhanced visual clarity, the residual dirty images are visualised on a linear scale, while all model estimate images and relative uncertainty images are displayed on a log₁₀ scale. Visual inspection suggests a general consistency of the reconstructions obtained with the different R2D2 models. Differences arise when examining faint emission with pixel values below 3 orders of magnitude from the peak, such as the tails of the jets and the surrounding of the inner core of the radio galaxy (highlighted via a red ellipse). In particular, both R2D2_{A₁, T₂} and R2D2_{A₂, T₂} appear to succeed in capturing more fine-scale structure than R2D2_{A₁, T₁}. We first focus on U-Net models. Comparing individual realisations of R2D2_{A₁, T₁} and R2D2_{A₁, T₂} reveals that certain faint features are missing in one that are recovered in the other. More specifically, three features are highlighted using arrows. The blue arrows indicate recovered features, while red arrows mark those that were not recovered. R2D2_{A₁, T₁} recovered two out of three features, the individual realisation of R2D2_{A₁, T₂} captured only one feature. This discrepancy is non-unexpected given the non-negligible uncertainty in these regions (see highlighted with black arrows in the relative uncertainty map). Interestingly, the mean image of R2D2_{A₁, T₂} recovers one more feature than the individual realisation (*i.e.* two out of three). Their presence in the mean image is more reliable than in individual realisations, as it results from averaging over two sources of epistemic uncertainty, reducing the influence of model-specific variations. We then turn our attention to U-WDSR models. All three highlighted features are consistently recovered in the images corresponding to both R2D2_{A₂, T₂} realisation and its mean image. The relative uncertainty images reveal a four-fold lower overall uncertainty for R2D2_{A₂, T₂} compared to R2D2_{A₁, T₂}. This supports the observation that differences between R2D2_{A₂, T₂} realisations and the mean image remain subtle. It also provides further confidence that all three features are real. Finally, analysis of the residual dirty images reveals a similar pattern of improvement across the three R2D2 models, where the new R2D2 models achieve higher data fidelity. Interestingly, the U-WDSR-based model enables a more homogenous residual structure than the U-Net-based R2D2 models, especially around the hotspots (highlighted in white circles), which are affected by calibration errors (Dabbech et al. 2021). This observation is validated numerically by the lower values of the data fidelity metrics (reported inside the associated images).

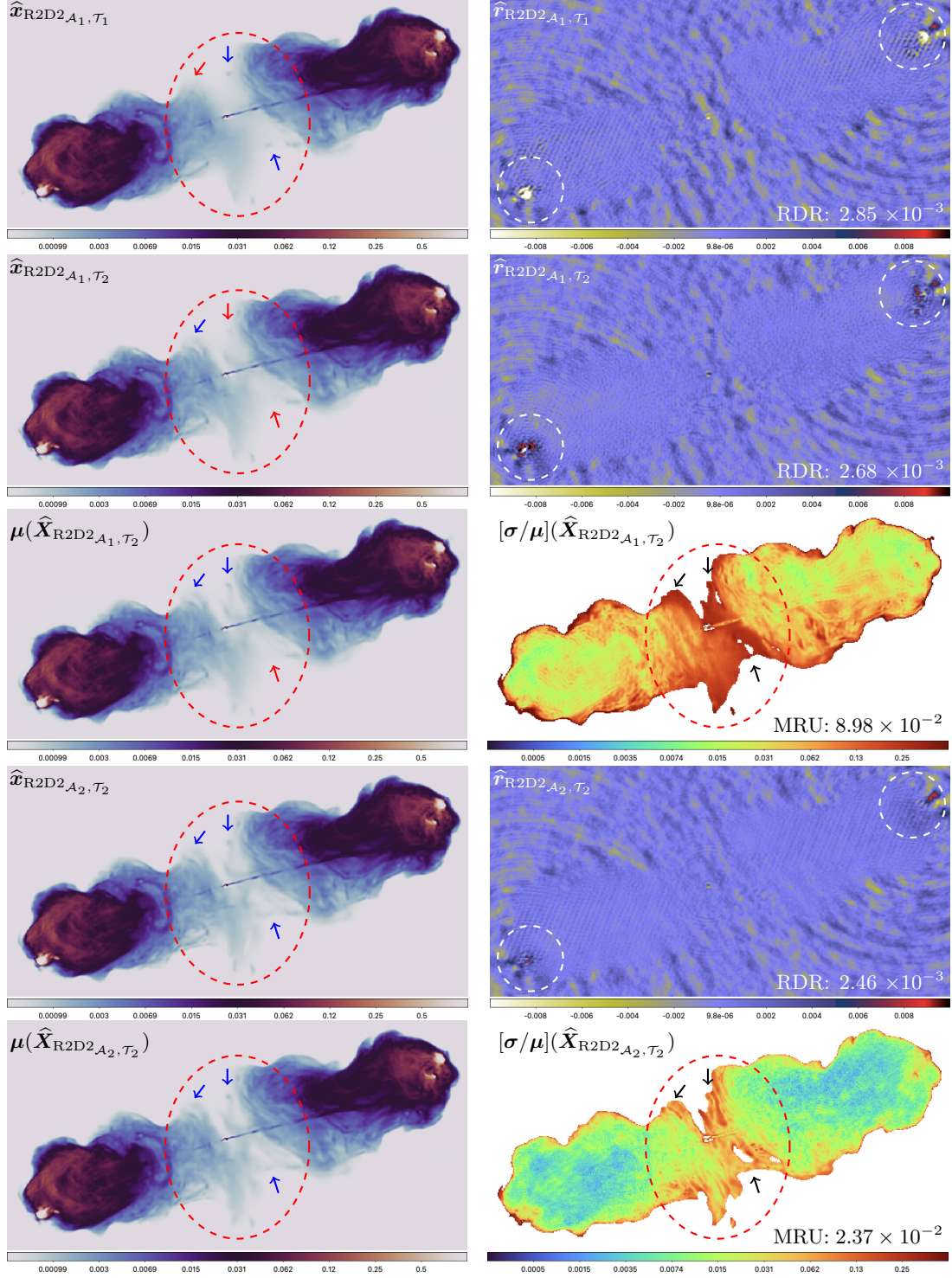


Figure 6. Cygnus A reconstruction results using R2D2 models. The first (resp. second and fourth) row shows the image estimate (left) and corresponding residual dirty image (right) obtained with a given realisation of $R2D2_{A_1, T_1}$ (resp. $R2D2_{A_1, T_2}$ and $R2D2_{A_2, T_2}$). The third (resp. fifth) row displays the mean image and associated relative uncertainty image delivered by $R2D2_{A_1, T_2}$ (resp. $R2D2_{A_2, T_2}$), and computed over $R = 25$ reconstructions (five different model realisations combined with five different values of ρ_{br}). The red ellipse in the image estimates and the relative uncertainty image highlights the region of faint emission. Coloured arrows highlight selected features, in blue to point towards a recovered feature, and in red to indicate its location when missing (in black inside relative uncertainty image). White circles in the residual dirty images indicate the locations of the hotspots. MRU and RDR metrics are reported inside the associated images.

6. CONCLUSIONS

This paper revisits and significantly enhances the R2D2 algorithm robustness for RI imaging, specifically under the VLA observational setting targeting the formation of 512×512 monochromatic intensity images. These advancements span three key areas: training methodologies, convergence criteria, and DNN architecture. The generalised training set introduces stochastic variations, including randomisation of the pixel resolution, visibility weighting parameter, sampling time, multi-noise, and multi-scan configurations—substantially improving the algorithm’s adaptability and robustness across diverse observational scenarios. To further enhance efficiency, a convergence criterion is introduced, whereby the reconstruction process is deemed complete and iterations stop once the data residuals align with the noise level, rather than continuing until a fixed maximum number of DNNs is reached. This approach reduces computational cost during reconstruction. It also improves training efficiency by pruning converged inverse problems, allowing subsequent DNNs to focus on unsolved inverse problems, leading to a more targeted optimisation. The core DNN architecture of the R2D2 algorithm is replaced with U-WDSR, a novel design, which offers enhanced imaging precision and improved robustness. The performance of the enhanced model R2D2 $_{\mathcal{A}_2, \mathcal{T}_2}$ was rigorously validated through comprehensive simulation setups. The results confirm that R2D2 $_{\mathcal{A}_2, \mathcal{T}_2}$ consistently outperforms AIRI and uSARA in image reconstruction quality while achieving comparable data fidelity with significantly fewer iterations, resulting in a much faster reconstruction process. Furthermore, R2D2 $_{\mathcal{A}_2, \mathcal{T}_2}$ exhibits much lower epistemic uncertainty compared to its U-Net-based counterpart, reaffirming the benefits of the U-WDSR architecture and the generalisation strategies introduced in this work. This enhanced robustness holds across both sources of epistemic uncertainty, namely multiple R2D2 series realisations and variation in visibility-weighting schemes. Illustration on real data consisting in VLA observations of Cygnus A further validates the model’s effectiveness and robustness in accounting for the epistemic uncertainty, with the U-WDSR-based R2D2 model recovering finer details and achieving superior data fidelity compared to the U-Net-based models. This work also introduces fully Python-based implementations of AIRI and uSARA, transitioning from MATLAB to a GPU-enabled Python framework. This transition not only improved computational efficiency but also enhanced the accessibility of the BASPLib library.

Future work will focus on extending these advancements to address the challenges posed by large-

scale imaging applications and adapting R2D2 for broader use cases. Specifically, future efforts will investigate (i) developing R2D2 for other telescopes or even a telescope-agnostic implementation, (ii) designing faceting strategies to enable seamless adaptation to any image size, including significantly larger dimensions, and (iii) generalising the approach to wideband polarisation imaging. These developments will position R2D2 as a robust and scalable solution, paving the way for its integration into next-generation radio telescopes like the SKA and beyond.

- 1 The authors would like to thank R.A. Perley for provid-
- 2 ing VLA observations of Cygnus A, and Adrian Jack-
- 3 son for his support related to Cirrus. This research
- 4 was supported by UK Research and Innovation through
- 5 the EPSRC grant EP/T028270/1 and the STFC grant
- 6 ST/W000970/1. Cirrus is a UK National Tier-2 HPC
- 7 Service at EPCC funded by the University of Edinburgh
- 8 and EPSRC (EP/P020267/1). The National Radio As-
- 9 tronomy Observatory is a facility of the National Sci-
- 10 ence Foundation operated under cooperative agreement
- 11 by Associated Universities, Inc.

Software: WSClean (Ofringa & Smirnov 2017), Meqtrees (Noordam & Smirnov 2010), BASPLib, PyTorch (Paszke et al. 2019), TorchKbNufft (Muckley et al. 2020), FINUFFT (Shih et al. 2021), PyNUFFT (Lin 2018);

Facilities: The Very Large Array (<https://public.nrao.edu/telescopes/vla/>); Cirrus (<https://www.cirrus.ac.uk/>).

DATA AVAILABILITY

R2D2 codes are available alongside AIRI and uSARA codes in the BASPLib code library on GitHub. BASPLib is developed and maintained by the Biomedical and Astronomical Signal Processing Laboratory (BASP). R2D2 DNN Series are available in the data set at doi: [10.17861/e3060b95-4fe6-4b61-9f72-d77653c305bb](https://doi.org/10.17861/e3060b95-4fe6-4b61-9f72-d77653c305bb).

Images used to generate training, validation, and testing datasets are sourced as follows. Optical astronomy images are gathered from NOIR-Lab/NSF/AURA/H.Schweiker/WIYN/T.A.Rector (University of Alaska Anchorage). Medical images are obtained from the NYU fastMRI Initiative database (Zbontar et al. 2018; Knoll et al. 2020). Radio astronomy images are obtained from the NRAO Archives, LOFAR HBA Virgo cluster survey (Edler et al. 2023), and LoTSS-DR2 survey (Shimwell et al. 2022). Observations of Cygnus A were provided by the National

Radio Astronomy Observatory (NRAO; Program code: 14B-336). The self-calibrated data can be shared upon request to R.A. Perley (NRAO).

REFERENCES

- Aghabiglou, A., San Chu, C., Dabbech, A., & Wiaux, Y. 2024, *ApJS*, 273, 3
- Aghabiglou, A., Terris, M., Jackson, A., & Wiaux, Y. 2023, in *Proc. IEEE ICASSP 2023*, 1–5
- Arras, P., Bester, H. L., Perley, R. A., et al. 2021, *A&A*, 646, A84
- Botteon, A., Shimwell, T., Cassano, R., et al. 2022, *A&A*, 660, A78
- Briggs, D. 1995, in *AAS*, Vol. 187, 112–02
- Carrillo, R. E., McEwen, J. D., & Wiaux, Y. 2012, *MNRAS*, 426, 1223
- Connor, L., Bouman, K. L., Ravi, V., & Hallinan, G. 2022, *MNRAS*, 514, 2614
- Cornwell, T. J. 2008, *IEEE J. Sel. Top. Signal Process.*, 2, 793
- Dabbech, A., Aghabiglou, A., San Chu, C., & Wiaux, Y. 2024, *ApJL*, 966, L34
- Dabbech, A., Repetti, A., Perley, R. A., Smirnov, O. M., & Wiaux, Y. 2021, *MNRAS*, 506, 4855
- Dabbech, A., Terris, M., Jackson, A., et al. 2022, *ApJL*, 939
- Edler, H., de Gasperin, F., Shimwell, T., et al. 2023, *A&A*, 676, A24
- Fessler, J., & Sutton, B. 2003, *IEEE Trans. Signal Process.*, 51, 560
- Geyer, F., Schmidt, K., Kummer, J., et al. 2023, *A&A*, 677, A167
- Högbom, J. 1974, *A&AS*, 15, 417
- Hotan, A., Bunton, J., Chippendale, A., et al. 2021, *PASA*, 38, e009
- Jonas, J. 2016, *Proc. Sci.*, MeerKAT Science: On the Pathway to the SKA, Sissa Trieste
- Knoll, F., Zbontar, J., Sriram, A., et al. 2020, *Radiol. Artif. Intell.*, 2, e190007
- Labate, M. G., Waterson, M., Alachkar, B., et al. 2022, *JATIS*, 8, 011024
- Lin, J.-M. 2018, *Journal of Imaging*, 4, 51
- Muckley, M. J., Stern, R., Murrell, T., & Knoll, F. 2020, in *ISMRM Workshop on Data Sampling & Image Reconstruction*
- Noordam, J. E., & Smirnov, O. M. 2010, *A&A*, 524, A61
- Offringa, A., McKinley, B., Hurley-Walker, N., et al. 2014, *MNRAS*, 444, 606
- Offringa, A. R., & Smirnov, O. 2017, *MNRAS*, 471, 301
- Onose, A., Carrillo, R. E., Repetti, A., et al. 2016, *MNRAS*, 462, 4314
- Onose, A., Dabbech, A., & Wiaux, Y. 2017, *MNRAS*, 469, 938
- Paszke, A., Gross, S., Massa, F., et al. 2019, preprint arXiv:1912.01703
- Repetti, A., & Wiaux, Y. 2020, in *Proc. IEEE ICASSP 2020*, 1434–1438
- Roth, J., Arras, P., Reinecke, M., et al. 2023, *A&A*, 678, A177
- Shih, Y.-h., Wright, G., Andén, J., Blaschke, J., & Barnett, A. H. 2021, in *2021 IEEE International Parallel and Distributed Processing Symposium Workshops (IPDPSW)*, IEEE, 688–697
- Shimwell, T., Hardcastle, M., Tasse, C., et al. 2022, *A&A*, 659, A1
- Swart, G. P., Dewdney, P. E., & Cremonini, A. 2022, *JATIS*, 8, 011021
- Terris, M., Dabbech, A., Tang, C., & Wiaux, Y. 2022, *MNRAS*, 518, 604
- Terris, M., Tang, C., Jackson, A., & Wiaux, Y. 2025, *MNRAS*, 537, 1608
- van Haarlem, M. P., Wise, M. W., Gunst, A., et al. 2013, *A&A*, 556, A2
- Wilber, A. G., Dabbech, A., Jackson, A., & Wiaux, Y. 2023, *MNRAS*, 522, 5558
- Yu, J., Fan, Y., Yang, J., et al. 2018, preprint arXiv:1808.08718
- Zbontar, J., Knoll, F., Sriram, A., et al. 2018, preprint arXiv:1811.08839